

NON-LINEAR REDUCED MODELING BY GENERALIZED KERNEL-BASED DYNAMIC MODE DECOMPOSITION

P. HÉAS^{†,*}, C. HERZET^{†,*}, AND B. COMBÈS^{‡,*}

Abstract. Reduced modeling of a computationally demanding dynamical system aims at approximating its trajectories, while optimizing the trade-off between accuracy and computational complexity. In this work, we propose to achieve such an approximation by first embedding the trajectories in a reproducing kernel Hilbert space (RKHS), which exhibits appealing approximation and computational capabilities, and then solving the associated reduced model problem. More specifically, we propose a new efficient algorithm for data-driven reduced modeling of non-linear dynamics based on linear approximations in a RKHS. This algorithm takes advantage of the closed-form solution of a low-rank constraint optimization problem while exploiting advantageously kernel-based computations. Reduced modeling with this algorithm reveals a gain in approximation accuracy, as shown by numerical simulations, and in complexity with respect to existing approaches.

Key words. Reduced modeling, kernel methods, low-rank approximations, non-linear dynamics

1. Introduction. Consider a high-dimensional system of the form:

$$\begin{cases} x_t(\theta) = f_t(x_{t-1}(\theta)), & t = 2, \dots, T, \\ x_1(\theta) = \theta, \end{cases} \quad (1.1)$$

where the x_t 's and θ in \mathbb{R}^p , constitute respectively a state trajectory and an initial condition, and where $f_t : \mathbb{R}^p \rightarrow \mathbb{R}^p$ is an arbitrary function whose direct evaluation is considered to be time consuming when p is large. Reduced modeling of dynamical systems (1.1) aims to lighten the computation load for the evaluation of a trajectory. Dynamic mode decomposition (DMD) [20] is a popular framework for this purpose. It consists in the data-driven linear approximation of function f_t : a matrix substituting f_t is learned from representative trajectories, so-called *snapshots*, by minimizing the norm of the residual of linear approximations subject to specific constraints [4, 13, 6].

This data-driven approach has been extended to reduced modeling of non-linear systems through a decomposition known as extended DMD (EDMD) [17, 23, 24, 25]. Basically, DMD and EDMD are identical, except that EDMD first immerses the trajectory through a non-linear mapping Ψ in a space exhibiting better approximation capabilities. More explicitly, let $\Psi : \mathbb{R}^p \rightarrow \mathcal{H}$, where \mathcal{H} is a Hilbert space endowed with the inner product $\langle \cdot, \cdot \rangle_{\mathcal{H}}$ and the induced norm $\| \cdot \|_{\mathcal{H}}$. EDMD approximates system (1.1) through a system taking the form of

$$\begin{cases} \eta_t(\theta) = \hat{A}_k \eta_{t-1}(\theta), & t = 2, \dots, T, \\ \eta_1(\theta) = \Psi(\theta), \end{cases} \quad (1.2)$$

where $\hat{A}_k : \mathcal{H} \rightarrow \mathcal{H}$ is a linear operator of rank at most k (satisfying some optimality criterion which will be specified later), yielding an approximation of the state $x_T(\theta)$ by an inverse mapping

$$\tilde{x}_T(\theta) = \Psi^{-1}(\eta_T(\theta)). \quad (1.3)$$

A proper definition of the inverse map Ψ^{-1} will be given in the next section.

^{*}INRIA, [†]IRMAR, [‡]IRISA, Univ. Rennes, 263 Av. Général Leclerc, Campus de Beaulieu, 35042 Rennes, France (patrick.heas@inria.fr, cedric.herzet@inria.fr, benoit.combes@inria.fr)
This paper is an improved and extended version of the conference proceeding [9].

In this paper, we will focus on reduced models of the form (1.2)-(1.3), where $\dim(\mathcal{H}) \gg p$ (including $\dim(\mathcal{H}) = \infty$). Such embeddings is appealing due to the ability of high-dimensional Hilbert spaces to linearize differential equations [14, 15, 18]. Nevertheless, computing a reduced model using these high-dimensional embeddings is difficult since neither the inference of operator \hat{A}_k nor the recursion (1.2) or the inversion (1.3) is tractable in a general setting.

To obtain a “good” trade-off between accuracy and complexity of the reduced model, one needs to accomplish two challenging tasks: *i*) learn a tractable representation of a low-rank operator \hat{A}_k yielding an accurate approximation of the form (1.2)-(1.3), *ii*) build a low-complexity algorithm able to compute $\tilde{x}_T(\theta)$ satisfying (1.2)-(1.3) for a given θ .

State-of-the-art methods *e.g.*, [22, 7, 11] involve a complexity in $\dim(\mathcal{H})$, thus are non-efficient in high-dimensional settings. Alternatively, authors in [24] have introduced an efficient algorithm to compute (1.3) for any map Ψ related to a reproducing kernel Hilbert space (RKHS) [21]. This algorithm known as kernel-based DMD (K-DMD) enjoys an advantageous complexity linear in p and independent of $\dim(\mathcal{H})$. Unfortunately, it relies on a set of restrictive assumptions.

In this work, we propose a new algorithm dubbed “generalized kernel-based DMD (GK-DMD)” that generalizes K-DMD to less restrictive assumptions, while being characterized by a gain in computational complexity and approximation accuracy, as evidenced by our numerical simulations.

The paper is organized as follows. Section 2 introduces the notations used in the paper, specifies the reduced modeling problem of interest and reviews existing solutions. Our generalized kernel-based algorithm is presented in Section 3. The proposed algorithm is evaluated numerically in Section 4. Proofs of theoretical results and technical details are provided in the appendices.

2. Problem and Existing Solutions.

2.1. Notations. We will need the following notations.

- The function space $\mathcal{B}(\mathcal{V}, \mathcal{U})$ is defined as the set of linear bounded operators from \mathcal{V} to \mathcal{U} . The subset $\mathcal{B}_k(\mathcal{V}, \mathcal{U}) = \{M \in \mathcal{B}(\mathcal{V}, \mathcal{U}) : \text{rank}(M) \leq k\}$ will be of particular interest.
- The adjoint of $A \in \mathcal{B}(\mathcal{V}, \mathcal{U})$ will be denoted $A^* \in \mathcal{B}(\mathcal{U}, \mathcal{V})$.
- For a vector $v \in \mathcal{V}$, the subscript notation v_i will denote its i -th component. The distinction from the subscript notation e_i denoting the i -th element of a set $\{e_i\}_{i>0}$ will be clear from the context.
- The SVD of $M \in \mathcal{B}_k(\mathcal{V}, \mathcal{U})$ will be denoted $M = \sum_{i=1}^k \sigma_i^M u_i^M \langle v_i^M, \cdot \rangle_{\mathcal{V}}$, where $\{u_i^M\}_{i=1}^k$, $\{v_i^M\}_{i=1}^k$ are respectively the left and right singular vectors associated to the sequence of decreasing singular values $\{\sigma_i^M\}_{i=1}^k$ of M . We will use the short-hand SVD notations: $M = U_M \Sigma_M V_M^*$, where $U_M \in \mathcal{B}(\mathbb{C}^k, \mathcal{U})$, $\Sigma_M \in \mathcal{B}(\mathbb{R}^k, \mathbb{R}^k)$ and $V_M^* \in \mathcal{B}(\mathcal{V}, \mathbb{C}^k)$ are defined for any vector $w \in \mathcal{V}$, $s \in \mathbb{C}^k$ as $U_M s = \sum_{j=1}^k u_j^M s_j$, $(V_M w)_i = \langle v_i^M, w \rangle_{\mathcal{V}}$ and $(\Sigma_M s)_i = \sigma_i^M s_i$.
- The pseudo inverse of M denoted $M^\dagger \in \mathcal{B}(\mathcal{U}, \mathcal{V})$ is defined as

$$M^\dagger = \sum_{i=1}^m (\sigma_i^M)^\dagger v_i^M \langle u_i^M, \cdot \rangle_{\mathcal{U}}, \quad \text{where} \quad (\sigma_i^M)^\dagger = \begin{cases} (\sigma_i^M)^{-1} & \text{if } \sigma_i^M > 0 \\ 0 & \text{else} \end{cases}.$$

Its SVD will be written in short-hand notations as $M^\dagger = V_M \Sigma_M^\dagger U_M^*$.

- The orthogonal projector onto the image of M (resp. of M^*) will be denoted by $\mathbb{P}_M = M M^\dagger$ (resp. $\mathbb{P}_{M^*} = M^\dagger M$) [5].

- The Hilbert-Schmidt norm $\|\cdot\|_{\mathcal{HS}}$ of an operator $M \in \mathcal{B}(\mathcal{V}, \mathcal{U})$ is defined as $\|M\|_{\mathcal{HS}}^2 = \sum_{i=1}^{\dim(\mathcal{V})} \|Me_i\|_{\mathcal{U}}^2$, where $\{e_i\}_{i=1}^{\dim(\mathcal{V})}$ is an orthonormal basis of \mathcal{V} . The ℓ_2 -norm of a vector $v \in \mathcal{V}$, with $\dim(\mathcal{V}) < \infty$, will be denoted $\|v\|_2$.

2.2. The Reduced Modeling Problem. In this work, we consider a data-driven approach: the reduced model is learned from a set of representative trajectories $\{x_t(\vartheta_i)\}_{t=1, i=1}^{T', N}$ of the high-dimensional system corresponding to N initial conditions $\{\vartheta_i\}_{i=1}^N$ and where T' is possibly different from T . We are interested in the design of an algorithm computing for any $\theta \in \mathbb{R}^p$ the approximation $\tilde{x}_T(\theta)$ using a reduced model of the form (1.2)-(1.3) satisfying the following definitions and conditions.

a) Low-rank Operator. The low-rank linear operator \hat{A}_k is identified as a solution of the constrained optimization problem

$$A_k^* \in \arg \min_{A \in \mathcal{B}_k(\mathcal{H}, \mathcal{H})} \|\Psi_{\mathbf{Y}} - A\Psi_{\mathbf{X}}\|_{\mathcal{HS}}, \quad (2.1)$$

where operators $\Psi_{\mathbf{X}}, \Psi_{\mathbf{Y}} \in \mathcal{B}(\mathbb{R}^m, \mathcal{H})$, with $m = N(T' - 1)$, are defined for any $w \in \mathbb{R}^m$ as the linear combinations

$$\Psi_{\mathbf{X}}w = \sum_{i,j=1}^{N, T'-1} \Psi(x_j(\vartheta_i))w_{(T'-1)(i-1)+j} \quad \text{and} \quad \Psi_{\mathbf{Y}}w = \sum_{i,j=1}^{N, T'-1} \Psi(x_{j+1}(\vartheta_i))w_{(T'-1)(i-1)+j}.$$

These combinations involve the training data set $\{x_j(\vartheta_i)\}_{i,j=1}^{N, T'}$, where the i -th component of a vector is denoted by subscript i . We remark that the square of the Hilbert-Schmidt norm in (2.1) can be rewritten as a sum of square norms of the form $\|\Psi(x_{j+1}(\vartheta_i)) - A\Psi(x_j(\vartheta_i))\|_{\mathcal{H}}^2$ over $j = 1, \dots, T' - 1$ and $i = 1, \dots, N$. Hence, the objective function in (2.1) measures the overall discrepancy between the true states and their prediction by operator A from the previous states, mapped into the Hilbert space. Operator (2.1) is a generalization of the solution of the minimization problem in [23, 24], subject to a low-rank constraint as in [4, 13].

b) Minimum Distance Estimation. The inverse map (1.3) from \mathcal{H} to \mathbb{R}^p is defined as a minimum distance estimate

$$\Psi^{-1}(\eta) \in \arg \min_{z \in \mathbb{R}^p} \|\eta - \Psi(z)\|_{\mathcal{H}}. \quad (2.2)$$

This definition of the inverse (2.2) is discussed in Appendix C.

c) Low-Complexity. The algorithm complexity is independent of $\dim(\mathcal{H})$ and the simulated trajectory length T .

Moreover, in order to enable the independence in T , we will assume all along this work that \mathcal{H} is separable and that A_k^* is diagonalizable¹. These assumptions enable to evaluate recursion (1.2) independently of the trajectory length T . Explicitly, let $\{\xi_i\}_{i \in \mathbb{N}}$ and $\{\zeta_i\}_{i \in \mathbb{N}}$ be bases of \mathcal{H} associated to the left and right eigen-vectors of A_k^* , i.e., $A_k^*\zeta_i = \lambda_i\zeta_i$ and $\xi_i A_k^* = \lambda_i\xi_i$ for $i \in \mathbb{N}$, where $\{\lambda_i\}_{i \in \mathbb{N}}$ is the related sequence of eigen-values sorted by decreasing magnitude. The finite rank of operator A_k^* (which has at most $\text{rank}(A_k^*) \leq k$ non-zero eigen-values) and the bi-orthogonality of the left and right eigen-vectors yield $A_k^*\Psi = \sum_{i=1}^k \lambda_i \langle \xi_i, \Psi \rangle_{\mathcal{H}} \zeta_i$. Defining $\varphi_i(\theta) = \langle \xi_i, \Psi(\theta) \rangle_{\mathcal{H}}$, (1.3) then becomes

¹ This assumption holds in particular if the linear bounded operator A_k^* is compact self-adjoint or normal [26], or in the case where $\dim(\mathcal{H}) < \infty$ and all non-zero eigen-values are distinct [12].

$$\tilde{x}_T(\theta) = \Psi^{-1} \left(\sum_{i=1}^k \nu_{i,T} \zeta_i \right), \quad \nu_{i,T} = \lambda_i^{T-1} \varphi_i(\theta). \quad (2.3)$$

Note that in the case where Ψ^{-1} is linear, then (2.3) simplifies to

$$\tilde{x}_T(\theta) = \sum_{i=1}^k \nu_{i,T} \mu_i, \quad \text{with} \quad \mu_i = \Psi^{-1} \zeta_i \in \mathbb{C}^p. \quad (2.4)$$

We mention that φ_i 's, μ_i 's and λ_i 's are known in the literature respectively as approximations of the i -th Koopman's *eigen-function*, *eigen-mode* and *eigen-value* [23].

2.3. Two Existing Solutions. In this section, we discuss two existing methods, each one of them fulfilling partially conditions *a*), *b*) and *c*) exposed in Section 2.2. They will serve as ingredients for our GK-DMD algorithm.

Optimal but Intractable. Reduced model (2.3) with A_k^* given by (2.1) is referred to as *low-rank EDMD*. A generalization of [6, Theorem 4.1] to separable infinite-dimensional Hilbert spaces provides a closed-form expression of operator A_k^* [8]: a solution of problem (2.1) for arbitrary value of k is

$$A_k^* = \mathbb{P}_{\mathbf{Z}^k} \Psi_{\mathbf{Y}} \Psi_{\mathbf{X}}^\dagger, \quad (2.5)$$

with the orthogonal projector $\mathbb{P}_{\mathbf{Z}^k} = \hat{P}_k \hat{P}_k^*$ and

$$\hat{P}_k \in \mathcal{B}(\mathbb{R}^k, \mathcal{H}) : w \rightarrow \sum_{i=1}^k u_i^{\mathbf{Z}} w_i, \quad (2.6)$$

where singular vectors $u_i^{\mathbf{Z}}$'s are issued from the SVD (see notations in Section 2.1) of

$$\mathbf{Z} = \Psi_{\mathbf{Y}} \mathbb{P} \Psi_{\mathbf{X}}^* \in \mathcal{B}(\mathbb{R}^m, \mathcal{H}). \quad (2.7)$$

It is worth noticing that for $k \geq m$, A_k^* boils down to

$$\hat{A}_k^{\ell s} = \Psi_{\mathbf{Y}} \Psi_{\mathbf{X}}^\dagger, \quad (2.8)$$

which is the solution of problem (2.1) without the low-rank constraint [22]. However, to achieve the low-complexity condition *c*) exposed in Section 2.2, it remains to propose a tractable algorithm to build and evaluate reduced model (2.3) from the closed-form, but potentially infinite-dimensional, solution A_k^* . Interestingly, the projector $\mathbb{P}_{\mathbf{Z}^k}$ in the closed-form solution (2.5) implies that $A_k^* \eta$, for any $\eta \in \mathcal{H}$, belongs to the span of operator $\Psi_{\mathbf{Y}}$. Therefore, an algorithm able to compute (2.3) by evaluation of scalar products of the form $\langle A_k^* \eta, \Psi(z) \rangle_{\mathcal{H}}$, where $z \in \mathbb{R}^p$, will have a complexity linear in the cost of the evaluation of a scalar product of the form $\langle \Psi(y_i), \Psi(z) \rangle_{\mathcal{H}}$, where the elements in the set $\{x_{t+1}(\vartheta_i)\}_{t=1, i=1}^{T'-1, N}$ define the columns $\{y_i\}_{i=1}^m$ of matrix $\mathbf{Y} \in \mathbb{R}^{p \times m}$. This idea constitutes the grounds of our algorithm presented in Section 3.2.

Tractable but Restrictive. To tackle the high-dimensional setting $\dim(\mathcal{H}) \gg p$, authors propose to consider in their seminal work a specific class of mapping [24]. They admit the mapping Ψ is such that a scalar product in \mathcal{H} of the form $\langle \Psi(z), \Psi(y) \rangle_{\mathcal{H}}$ with $z, y \in \mathbb{R}^p$ is given by the evaluation of a symmetric positive definite kernel

$$h : \mathbb{R}^p \times \mathbb{R}^p \rightarrow \mathbb{R}; \quad (y, z) \rightarrow h(y, z) = \langle \Psi(y), \Psi(z) \rangle_{\mathcal{H}}.$$

According to the Moore-Aronszajn theorem, there is a unique Hilbert space of functions on \mathbb{R}^p , called a reproducing kernel Hilbert space (RKHS) [21], for which h is a symmetric positive definite kernel so-called reproducing kernel. The advantage of such a construction is that the kernel trick² can be used to compute inner products in the RKHS \mathcal{H} with a complexity equal to that required to evaluate the kernel h , which is in general independent of $\dim(\mathcal{H})$ [2]. The key idea of their method called K-DMD is to use the kernel trick to evaluate inner products with eigen-vectors of $\hat{A}_k^{\ell s}$. Assuming that the complexity for the evaluation of the kernel is $\mathcal{O}(p)$, the overall complexity of the K-DMD algorithm is independent of $\dim(\mathcal{H})$ and T , *i.e.*, fulfills condition *c*).

However, as proposed in [24], K-DMD computes an approximation of reduced model (2.3) under restrictive assumptions. In particular the four following assumptions are needed: *i*) the low-rank constraint in (2.1) is ignored, *i.e.*, $A_k^* = \hat{A}_k^{\ell s}$ defined in (2.8); *ii*) the operator $\Psi_{\mathbf{X}}$ is full-rank; *iii*) Ψ^{-1} is linear; *iv*) the $\Psi^{-1}\zeta_j$'s belong to the span of \mathbf{Y} . The reduced model computed by K-DMD is therefore not optimal in the sense of definitions *a*) and *b*) given in Section 2.2. A description of the algorithm is provided in Appendix A.

3. A Generalized Kernel-Based Algorithm. Our algorithm called GK-DMD computes the low-rank reduced model (2.3) for \mathcal{H} being an RKHS, with a complexity independent of $\dim(\mathcal{H})$ and T and is relieved from the assumptions made in K-DMD. As for K-DMD, the GK-DMD exploits the kernel-trick and resorts to an analogous computation of eigen-functions. Its main innovation in comparison to the latter state-of-the-art algorithm is that GK-DMD computes reduced model (2.3) based on the exact solution (2.5) of problem (2.1). In other words, the proposed GK-DMD algorithm fulfills definitions *a*) and *b*), as well as the low-complexity condition *c*) exposed in Section 2.2. The GK-DMD algorithm is given in Algorithm 1 and will be presented extensively in Section 3.2. In a nutshell, it consists in an off-line part, which computes a low-dimensional representation of A_k^* , and in a on-line part that uses the latter to evaluate an approximated trajectory for a given initial condition. More specifically, it relies on the two following original results:

- the right and left eigen-vectors of the optimal operator A_k^* belong to a low-dimensional sub-space of \mathcal{H} ; their low-dimensional representations are tractable and computed using the kernel function; this result is detailed in Section 3.1.1;
- the inverse map defined in (2.2) involves a distance minimization problem in \mathcal{H} ; taking advantage that, in reduced model (2.3), the argument of the inverse belongs to a low-dimensional subspace of \mathcal{H} , the high-dimensional minimization problem boils down to a tractable p -dimensional optimization problem; this result is detailed in Section 3.1.2.

3.1. Main Results.

3.1.1. Low-Dimensional Representation of A_k^* . Our algorithm relies on the following proposition. Its proof is detailed in Appendix B. Let $\{\xi_i\}_{i=1}^k$ and $\{\zeta_i\}_{i=1}^k$ denote the left and right eigen-vectors of A_k^* associated to its at most k non-zero eigen-values $\{\lambda_i\}_{i=1}^k$.

² Let us illustrate the kernel trick with the polynomial kernel $h(y, z) = (1 + y^*z)^2$ and $p = 2$. The kernel maps \mathbb{R}^2 onto the RKHS $\mathcal{H} = \mathbb{R}^6$. Expanding the kernel, we obtain $h(y, z) = (1 + y^*z)^2 = 1 + 2y_1z_1 + 2y_2z_2 + 2y_1y_2z_1z_2 + y_1^2z_1^2 + y_2^2z_2^2$, where $y = (y_1 \ y_2)^*$ and $z = (z_1 \ z_2)^*$ in \mathbb{R}^2 so that we have $h(y, z) = \Psi(y)^*\Psi(z)$, with $\Psi(y) = (1 \ \sqrt{2}y_1 \ \sqrt{2}y_2 \ \sqrt{2}y_1y_2 \ y_1^2 \ y_2^2)^* \in \mathbb{R}^6$. Therefore, we can evaluate an inner product of vectors in \mathcal{H} by computing a function of an inner product in \mathbb{R}^2 .

PROPOSITION 3.1. For $i = 1, \dots, k$, the left and right eigen-vectors of A_k^* and its eigen-values satisfy $\xi_i = U_{\Psi_X} \tilde{\xi}_i$, $\zeta_i = \hat{P}_k \tilde{\zeta}_i$ and $\lambda_i = \tilde{\lambda}_i$ where $\{(\tilde{\xi}_i, \tilde{\lambda}_i)\}_{i=1}^k$ and $\{(\tilde{\zeta}_i, \tilde{\lambda}_i)\}_{i=1}^k$ denote respectively the first k right eigen-vectors and eigen-values of the matrices in $\mathbb{R}^{m \times m}$

$$R \Psi_Y^* \Psi_Y S_k^* S_k \Psi_Y^* \Psi_X R^* \quad \text{and} \quad S_k \Psi_Y^* \Psi_Y R^* R \Psi_X^* \Psi_X S_k^*, \quad (3.1)$$

where $R = \Sigma_{\Psi_X}^\dagger V_{\Psi_X}^*$ and $S_k = \text{diag}((\sigma_1^Z)^\dagger \dots (\sigma_k^Z)^\dagger 0 \dots 0) V_Z^*$.

This proposition gives a closed-form decomposition for the ξ_i 's and the ζ_i 's, the left and right eigen-vectors of the optimal solution A_k^* given in (2.5) and supplies the related eigen-values λ_i 's. The decompositions involve operator \hat{P}_k defined in (2.6) and operator U_{Ψ_X} appearing in the short-hand notation of the SVD of Ψ_X . A consequence of this proposition is that parameters $\{(\xi_i, \zeta_i, \lambda_i)\}_{i=1}^k$ of reduced model (2.3) can be written in terms of their low-dimensional counterpart $\{(\tilde{\xi}_i, \tilde{\zeta}_i, \tilde{\lambda}_i)\}_{i=1}^k$. We notice that the first k left and right eigen-vectors of A_k^* are normalized, *i.e.*, that for $i = 1, \dots, k$ the condition $\zeta_i^* \xi_i = 1$ stands, if

$$\tilde{\zeta}_i^* E \tilde{\xi}_i = 1, \quad (3.2)$$

with $E = S_k \Psi_Y^* \Psi_X R^*$. This normalization condition can be verified using some algebraic calculus. We ensure condition (3.2) for $i = 1, \dots, k$ by first computing the complex number $\gamma_i = \tilde{\zeta}_i^* E \tilde{\xi}_i$ and then rescaling the eigen-vector $\tilde{\zeta}_i$ by γ_i^{-1} .

3.1.2. Kernel-Based Inversion. The low-dimensional representation of eigen-vectors of A_k^* provided in Proposition 3.1 constitutes an essential ingredient of the GK-DMD algorithm. However, to achieve the design of this algorithm, it remains to provide a feasible manner to evaluate Ψ^{-1} in (2.3). Once more, the idea consists in relying on the kernel trick in order to evaluate the inverse with a complexity independent of $\dim(\mathcal{H})$.

We first deduce from Proposition 3.1 the closed-form i -th eigen-function approximation $\varphi_i(\theta)$ for $i = 1, \dots, k$ at any point $\theta \in \mathbb{R}^p$ given by

$$\varphi_i(\theta) = \langle \xi_i, \Psi(\theta) \rangle_{\mathcal{H}} = \tilde{\xi}_i^* R \Psi_X^* \Psi(\theta). \quad (3.3)$$

Then, relying again on Proposition 3.1, we can rewrite the reduced model (2.3) in terms of $\tilde{\zeta}_i$'s, $\varphi_i(\theta)$'s and $\tilde{\lambda}_i$'s as

$$\tilde{x}_T(\theta) = \Psi^{-1} \left(\sum_{j=1}^k \hat{P}_k \tilde{\zeta}_j \tilde{\lambda}_j^{T-1} \varphi_j(\theta) \right) = \Psi^{-1} (\Psi_Y g^{\theta, T}), \quad (3.4)$$

$$\text{with } g^{\theta, T} = S_k^* (\tilde{\zeta}_1 \dots \tilde{\zeta}_k) \begin{pmatrix} \tilde{\lambda}_{\ell, 1}^{T-1} \varphi_1(\theta) & \dots & \tilde{\lambda}_{\ell, k}^{T-1} \varphi_k(\theta) \end{pmatrix}^* \in \mathbb{R}^m. \quad (3.5)$$

Equation (3.4) implies the inverse of a linear combination of the $\Psi(y_i)$'s, where $y_i = x_{t+1}(\vartheta_j)$ with $i = (T' - 1)j + t$ for $j = 1, \dots, N$ and $t = 1, \dots, T' - 1$. From (2.2), we rewrite the inverse of the linear combination appearing in (3.4) in terms of scalar products in \mathcal{H} computable using the kernel trick, *i.e.*, given the kernel h ,

$$\begin{aligned} \tilde{x}_T(\theta) &\in \arg \min_{z \in \mathbb{R}^p} \|\Psi_Y g^{\theta, T} - \Psi(z)\|_{\mathcal{H}} = \arg \min_{z \in \mathbb{R}^p} \|\Psi_Y g^{\theta, T} - \Psi(z)\|_{\mathcal{H}}^2 \\ &= \arg \min_{z \in \mathbb{R}^p} \|\Psi(z)\|_{\mathcal{H}}^2 - 2 \langle \Psi_Y g^{\theta, T}, \Psi(z) \rangle_{\mathcal{H}} \\ &= \arg \min_{z \in \mathbb{R}^p} \left(h(z, z) - 2 \sum_{i=1}^m g_i^{\theta, T} h(y_i, z) \right). \end{aligned} \quad (3.6)$$

Sufficient conditions for the existence of minimizer (3.6) are provided and discussed for various kernel choices in Appendix C. A minimizer (3.6) can be computed (up to some accuracy) using standard optimization methods with a complexity independent of $\dim(\mathcal{H})$. Moreover, the gradient of the objective is in general closed-form, which enables the use of efficient large-scale optimization techniques such as limited memory quasi-newton methods [19]. In this case, the complexity to compute the inverse is linear in p .

Algorithm 1 : GK-DMD

• Off-line.

Inputs: $x_t(\vartheta_i)$'s

- 1) Compute matrices $\Psi_X^* \Psi_X$, $\Psi_Y^* \Psi_Y$, $\Psi_Y^* \Psi_X$ in $\mathbb{R}^{m \times m}$ with the kernel trick.
- 2) Compute $(V_{\Psi_X}, \Sigma_{\Psi_X})$ by eigen-decomposition of $\Psi_X^* \Psi_X$.
- 3) Compute (V_Z, Σ_Z) by eigen-decomposition of $Z^* Z$ with Z given by (2.7).
- 4) Compute the two matrices given in Proposition 3.1 and compute their eigen-vector/eigen-value couples $\{(\tilde{\xi}_i, \tilde{\lambda}_i)\}_{i=1}^k$ and $\{(\tilde{\zeta}_i, \tilde{\lambda}_i)\}_{i=1}^k$.
- 5) Rescale each right eigenvector $\tilde{\zeta}_i$ by factor $(\tilde{\zeta}_i^* E \tilde{\xi}_i)^{-1}$ with $E = S_k \Psi_Y^* \Psi_X R^*$.

Outputs: R , S_k , $\tilde{\xi}_i$'s, $\tilde{\zeta}_i$'s and $\tilde{\lambda}_i$'s

• On-line.

Inputs: off-line outputs and θ

- 6) Compute $\Psi_X^* \Psi(\theta)$ in \mathbb{R}^m with the kernel trick.
- 7) Compute eigen-functions $\{\varphi_i(\theta)\}_{i=1}^k$ defined in (3.3).
- 8) Compute $\tilde{x}_T(\theta)$ solving (3.6);

Output: $\tilde{x}_T(\theta)$.

3.2. The GK-DMD Algorithm. We begin by detailing the off-line computation. According to Proposition 3.1, the low-dimensional representation of the right and left eigen-vectors, and the associated eigen-values of the optimal operator A_k^* are obtained by eigen-decomposition of matrices given in (3.1). As detailed hereafter, the five first steps of the algorithm precisely compute this low-dimensional representation. Relying on the kernel function, step 1) first computes the inner products in \mathcal{H} needed to build matrices $\Psi_X^* \Psi_X$, $\Psi_Y^* \Psi_Y$, $\Psi_Y^* \Psi_X$ in $\mathbb{R}^{m \times m}$. In steps 2) and 3), the matrices R and S_k in $\mathbb{R}^{m \times m}$ are obtained by eigen-decomposition of $\Psi_X^* \Psi_X$ and $Z^* Z$ belonging also to $\mathbb{R}^{m \times m}$. These three first steps enable to obtain matrices given in (3.1) by simple matrix products. Step 4) of the algorithm computes the right and left eigen-vectors and the associated eigen-values of matrices given in (3.1). Step 5) finally normalizes the latter eigen-vectors, as detailed in Section 3.1.1.

In the on-line part of the algorithm, the low-dimensional representation given by the outputs of the off-line part is exploited to compute the reduced model output $\tilde{x}_T(\theta)$, for a given initial condition θ . As discussed in Section 3.1.2, the computation of $\tilde{x}_T(\theta)$ is obtained by solving the p -dimensional optimization problem (3.6). The objective function of this problem depends on kernel functions weighted by the m -dimensional coefficient vector $g^{\theta, T}$ defined in (3.5). This vector depends itself on the low-dimensional representation of operator A_k^* computed in the off-line part and on the eigen-functions $\{\varphi_i(\theta)\}_{i=1}^k$. These eigen-functions are obtained in steps 6) and 7) of the algorithm : step 6) uses the kernel trick to compute the m -dimensional vector $\Psi_X^* \Psi(\theta)$ while step 7) deduces the eigen-functions (3.3) using the low-dimensional representation. With these eigen-functions, we then compute the vector component $g_i^{\theta, T}$ weighting the kernel function $h(y_i, z)$ in the objective function of (3.6). Step 8)

finally solves this optimization problem and provides reduced model $\tilde{x}_T(\theta)$.

3.3. Theoretical Performance Analysis. In this section, we begin by analyzing the advantage of the GK-DMD algorithm in terms of computational complexity and then show that the approximation error is optimal in some sense in the RKHS. Moreover, we show that the norm of the learning approximation error is tractable without any increase of the algorithm complexity.

3.3.1. Complexity. Assuming a complexity $\mathcal{O}(p)$ for the evaluation of the kernel function³, the overall complexity of the proposed algorithm scales in $\mathcal{O}(m^2(m+p))$, just as for K-DMD, as detailed in Appendix A. We remark that this complexity is independent of T thanks to the eigen diagonalization of A_k^* , and independent of $\dim(\mathcal{H})$ due to the use of the kernel-trick in the first and last steps of the algorithm. Reduced modeling is very concerned by the on-line computational cost, *i.e.*, complexity of computation steps depending on the input θ . As $k \leq m \leq p$ and typically $k \ll p$, GK-DMD is attractive by its on-line complexity in $\mathcal{O}(m^2k + mp)$, thus it scales linearly with respect to the dimension of the reduced model k or the ambient dimension p , in comparison to $\mathcal{O}(m^2p)$ operations for K-DMD. Indeed, the matrix-vector product $\Psi_{\mathbf{X}}^* \Psi(\theta)$ in step 6) and the inversion in step 8) are both computed in $\mathcal{O}(pm)$ operations, while eigen-functions in step 7) require $\mathcal{O}(m^2k)$ operations.

3.3.2. Learning Accuracy. The learning error of our GK-DMD algorithm is optimal in the sense it is equal to the minimal Hilbert-Schmidt norm of the error achievable in the RKHS for the minimization problem (2.1). The norm of this optimal error, given by a generalization of [6, Theorem 4.1] to separable infinite-dimensional Hilbert spaces, is closed-form

$$\|\Psi_{\mathbf{Y}} - A_k^* \Psi_{\mathbf{X}}\|_{\mathcal{HS}}^2 = \sum_{i=k+1}^m (\sigma_i^{\mathbf{Z}})^2 + \sum_{i=i^*}^m \sum_{j=1}^m (\sigma_j^{\Psi_{\mathbf{Y}}})^2 \left((v_j^{\Psi_{\mathbf{Y}}})^* v_i^{\Psi_{\mathbf{X}}} \right)^2, \quad (3.7)$$

with $i^* = \text{rank}(\Psi_{\mathbf{X}}) + 1$ [8].

Moreover, it is worth noticing that the optimal error norm (3.7) is tractable. It possibly involves a little extra computation which does not increase the complexity of Algorithm 1. More precisely, we notice that the left singular vectors $\{v_i^{\Psi_{\mathbf{X}}}\}_{i=1}^m$ and $\{v_i^{\mathbf{Z}}\}_{i=1}^m$ respectively of $\Psi_{\mathbf{X}}$ and \mathbf{Z} and their associated singular values $\{\sigma_i^{\Psi_{\mathbf{X}}}\}_{i=1}^m$ and $\{\sigma_i^{\mathbf{Z}}\}_{i=1}^m$ have been precomputed in step 2) and 3) of the algorithm. We distinguish the two following cases depending on the value of i^* , which equals to the number of non-zero singular values in the set $\{\sigma_i^{\Psi_{\mathbf{X}}}\}_{i=1}^m$ plus one.

- If $i^* = m + 1$, *i.e.*, $\Psi_{\mathbf{X}}$ is full rank, the second term on the right-hand side vanishes, and the error norm is directly computable.
- Otherwise, in order to evaluate the error norm, we need to make the extra computation of the left singular vectors $\{v_i^{\Psi_{\mathbf{Y}}}\}_{i=1}^m$ and singular values $\{\sigma_i^{\Psi_{\mathbf{Y}}}\}_{i=1}^m$ of $\Psi_{\mathbf{Y}}$. They are obtained by eigen-decomposition of matrix $\Psi_{\mathbf{Y}}^* \Psi_{\mathbf{Y}} \in \mathbb{R}^{m \times m}$, precomputed using the kernel trick in step 1) of the algorithm. This additional eigen-decomposition will involve a complexity in $\mathcal{O}(m^3)$, *i.e.*, preserves the global algorithm complexity in $\mathcal{O}(m^2(m+p))$.

4. Numerical Simulations. In this section, we assess four data-driven reduced modeling methods for the approximation of two high-dimensional systems.

³This property is true for most standard kernels, *e.g.*, polynomial or Gaussian kernels [2].

	LR-DMD	TLS-DMD	K-DMD	GK-DMD
off-line	$\mathcal{O}(m^2(m+p))$	$\mathcal{O}(m^2(m+p))$	$\mathcal{O}(m^2(m+p))$	$\mathcal{O}(m^2(m+p))$
on-line	$\mathcal{O}(pk)$	$\mathcal{O}(Tpm)$	$\mathcal{O}(pm^2)$	$\mathcal{O}(pm + m^2k)$

TABLE 4.1

Off-line and on-line complexities of reduced modeling algorithms. We recall that p is the ambient state dimension, k is the reduced model dimension, T is the predicted trajectory length and m is the size of the training data set.

4.1. Experimental Setup and Evaluation Benchmark. Our benchmark consists of the four following algorithms:

- low-rank DMD (LR-DMD) [6, Algorithm 3],
- total-least-square DMD (TLS-DMD) [11],
- kernel-based DMD (K-DMD) [24],
- the proposed generalized kernel DMD (GK-DMD), *i.e.*, Algorithm 1.

Table 4.1 summarizes the off-line and on-line complexities of the different algorithms. For the K-DMD and GK-DMD algorithms, we use a quadratic polynomial kernel or a Gaussian kernel with a standard deviation of 10 [2]. Details on these kernels are provided in Appendix C.3.

These algorithms are used to approximate two high-dimensional models.

- A Rayleigh-Bénard convection [3] model, which is a standard benchmark in meteorology. Convection is driven by two coupled partial differential equations. After discretization of these equations, we obtain a discrete system with $p = 4096$ for the evolution of vorticity and temperature fields on a grid of size 64×32 .
- A divergence-free fractional Brownian motion (fBm) evolution model, which is inspired by the turbulence phenomenology. It aims to evaluate the capability of reduced modeling methods to capture the fractal structure of vortices. The initial states of dimension $p = 512$ are bi-dimensional divergence-free fBm vector fields on a square grid 16×16 . Vector field evolution is driven by a discrete system according to a diffusive quadratic model.

A precise description of these high-dimensional systems, together with details on the experimental setting used in our numerical simulations, are provided in Appendix D.

We study the evolution with respect to the rank k of the

- **reconstruction error**

$$\epsilon_{rec} = \left(\sum_{j=1}^{N_\theta} \sum_{t=1}^{T-1} \frac{\|\tilde{x}_2(x_t(\theta_j)) - x_{t+1}(\theta_j)\|_2^2}{\|x_{t+1}(\theta_j)\|_2^2} \right)^{1/2},$$

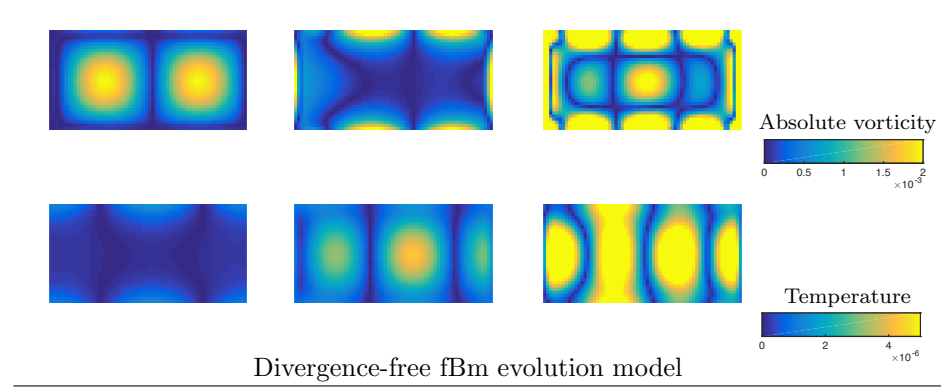
for a set of initial conditions $\{\theta_j\}_{j=1}^{N_\theta}$; it measures the overall discrepancy between the true state $x_{t+1}(\theta_j)$ at time $t+1$ and the approximated state $\tilde{x}_2(x_t(\theta_j))$ predicted with the reduced model from the true state at time t for $t = 1, \dots, T-1$;

- **learning error**

$$\epsilon_{learn} = \left(\sum_{j=1}^N \sum_{t=1}^{T'-1} \frac{\|\tilde{x}_2(x_t(\vartheta_j)) - x_{t+1}(\vartheta_j)\|_2^2}{\|x_{t+1}(\vartheta_j)\|_2^2} \right)^{1/2};$$

it measures the overall discrepancy between the state $x_{t+1}(\vartheta_j)$ and the prediction $\tilde{x}_2(x_t(\vartheta_j))$ at time t for $t = 1, \dots, T'-1$; it reveals the capability of the reduced model to reproduce the snapshots used during the learning stage.

Rayleigh-Bénard convection



Divergence-free fBm evolution model

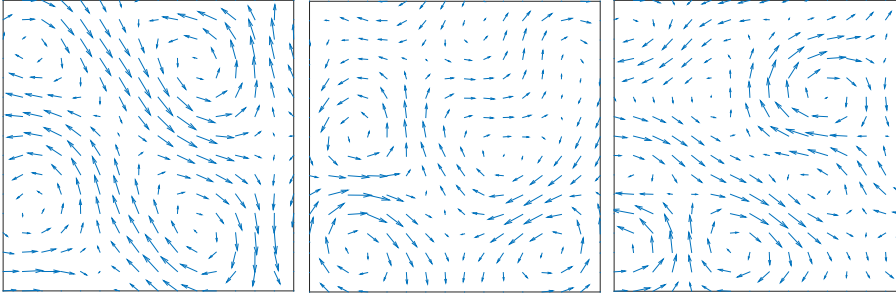


FIG. 4.1. Three examples of snapshot $x_t(\vartheta_j)$: maps of absolute vorticity and temperature generated by Rayleigh-Bénard convection (above); motion fields generated by the divergence-free fBm evolution model (below).

We mention that a small learning error ϵ_{learn} will not necessarily yield a small reconstruction error ϵ_{rec} . A small ϵ_{learn} may be related to model overfitting. The learning error will nonetheless help to understand the behavior of the different methods.

The size of the training data is set to $m = 90$ for the two high-dimensional systems. The experimental setup is as follows.

- For the Rayleigh-Bénard convection model, 10 initial conditions ϑ_j are sampled from a uniform distribution on an hyper-cube in \mathbb{R}^5 parametrizing solutions of the Lorenz attractor [16]. Then using ϑ_j to initialize the dynamic model (presented in Appendix D), we compute trajectories for $t = 1, \dots, 10$ (resulting in 100 states $x_t(\vartheta_j)$). Examples of $x_t(\vartheta_j)$'s are displayed in Figure 4.1. We design the test data in order to evaluate the capability of the reduced models to perform predictions for the Rayleigh-Bénard convection model, which is known to be chaotic [3, 16]. Therefore, we set the test data as the prolongation of the training data trajectories: the 10 initial conditions are $\theta_j = x_{10}(\vartheta_j)$ and trajectories $x_t(\theta_j)$ for $t = 1, \dots, 10$ are computed in the same way as for the training data set.
- For the divergence-free fBm evolution model, 100 noisy fBms vector fields ϑ_j are used as initial conditions. More precisely, fBms vector fields are drawn using the wavelet representation proposed in [10, Proposition 3.1] with 18 fractional wavelet coefficients and then corrupt by a weak additional Gaussian white noise (peak signal-to-noise ratio of 130). We then compute trajectories for $t = 1, 2$ (resulting in 100 states $x_t(\vartheta_j)$) using the quadratic dynamical model (presented in Appendix D). Examples of $x_t(\vartheta_j)$'s are displayed in Figure 4.1. The test data set is generated in the same way.

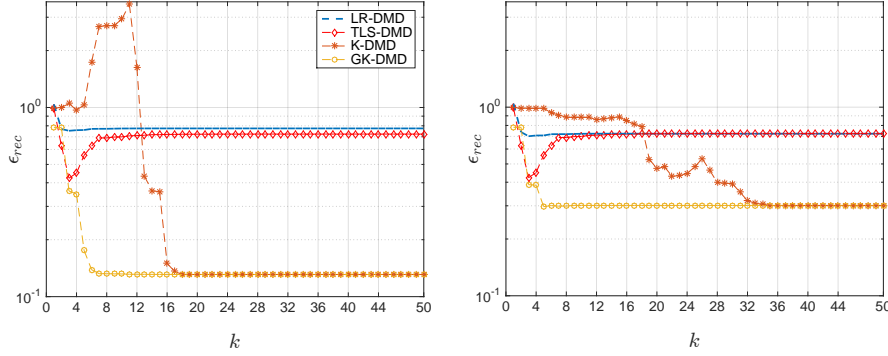


FIG. 4.2. Evaluation of reconstruction error ϵ_{rec} as a function of the rank k for the approximation of a Rayleigh-Bénard convective system using Gaussian (left) and polynomial (right) kernels.

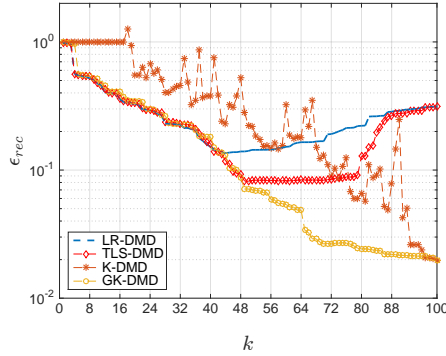


FIG. 4.3. Evaluation of the reconstruction error ϵ_{rec} as a function of the dimension k for the approximation of a divergence-free fBm evolution model using a Gaussian kernel.

4.2. Results.

4.2.1. Analysis of Accuracy v.s. Rank of Approximation. The reconstruction error ϵ_{rec} is evaluated as a function of the reduced model dimension for the approximation of the two high-dimensional systems. Plots comparing the four algorithms are presented in Figure 4.2 and Figure 4.3, respectively for the Rayleigh-Bénard convection and for the divergence-free fBm evolution. Overall, we observe that GK-DMD outperforms almost everywhere the other methods.

Rayleigh-Bénard convection. We first discuss the results shown in Figure 4.2 for the Gaussian kernel. While K-DMD and GK-DMD perform similarly for $k \geq 18$, GK-DMD exhibits for $k < 18$ a clear gain in accuracy compared to the other methods reaching almost a decade. The gain in accuracy between K-DMD and GK-DMD may be due to the fact that GK-DMD computes exactly reduced model (2.3), and in particular considers A_k^* instead of $\hat{A}_k^{\ell s}$. Besides, as $\text{rank}(\Psi_{\mathbf{X}}^* \Psi_{\mathbf{X}}) = m$, i.e., operator $\Psi_{\mathbf{X}}$ is full-rank, similar performances of the two kernel-based methods in the case where $k \geq 18$ can be explained by the fact that the low-rank constraint becomes inactive (implying that $\hat{A}_k^{\ell s} = A_k^*$), Ψ^{-1} is well approximated by a linear mapping and furthermore the $\Psi^{-1}\zeta_j$'s are well represented in the span of \mathbf{Y} . A lower value on the accuracy is reached around k slightly greater than 5, suggesting that a linear model can explain only 5 components in \mathcal{H} . Similar results are obtained with a polynomial kernel. Nevertheless, for K-DMD and GK-DMD, the reconstruction error is higher with polynomials than for Gaussian kernels, revealing that their performance is kernel-

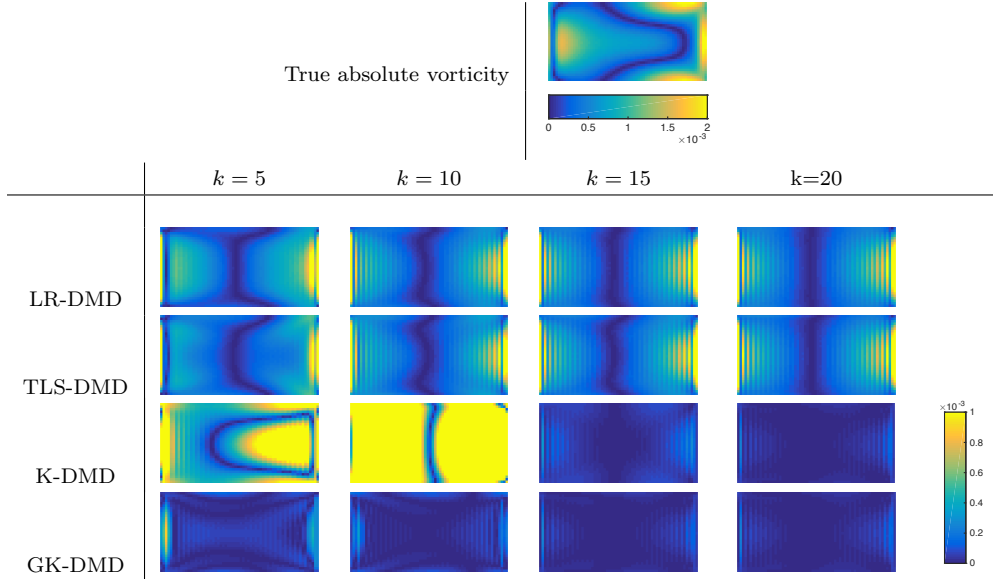


FIG. 4.4. Reconstruction error maps of the different reduced models for increasing value of k . The image above represents the absolute vorticity field $x_2(\theta)$, while each image in the table below represents the absolute vorticity of the bi-variate field $\tilde{x}_2(\theta) - x_2(\theta)$, for a typical initial condition θ .

dependent. The problem of the kernel choice, and more generally the inference of a relevant mapping Ψ , is an open question out of the scope of this paper. We refer the interested reader to recent works on this issue [17, 25].

Additionally, the reconstruction errors of GK-DMD, LR-DMD and TLS-DMD are comparable for $k < 4$. Nevertheless, the accuracy of LR-DMD and TLS-DMD reaches a lower bound around $k \simeq 4$ and then deteriorates as k increases or reaches an asymptote, suggesting data overfitting. This undesirable effect will be discussed in the numerical experiences of Section 4.2.3.

Divergence-free fBm evolution. We now turn to the reduction of our simplified turbulence model. Results shown in Figure 4.3 are in agreement with observations made in the case of the Rayleigh-Bénard convection. In particular the gain in accuracy in comparison to state-of-the-art methods reaches a peak of more than a decade at $k = 89$. However, we can point out two important differences with the previous results shown in Figure 4.2. First, while the GK-DMD error is a monotonic strictly decreasing function with respect to the dimension k , K-DMD has a plateau up to $k \sim 20$ and then is chaotic before reaching the GK-DMD performance near the point $k = m$. It is not clear how the K-DMD error behavior can be interpreted. The only conclusion that can be drawn is that GK-DMD provides a preferable reduced model, in the sense that approximation becomes increasingly accurate as k grows. Second, LR-DMD and TLS-DMD operate in a very similar way as GK-DMD up to $k \sim 40$, but the accuracy of these methods then deteriorate significantly as k increases. As already observed for the Rayleigh-Bénard model, overfitting at the learning stage is likely to be the explanation to this performance loss of these state-of-the-art algorithms. This issue is further discussed in Section 4.2.3.

4.2.2. Analysis of Error Maps. To complement the quantitative evaluation performed in Section 4.2.1, we proceed to the visual inspection of the spatial distribution of the error. Typical error maps are shown in Figure 4.4 and Figure 4.5. Figure 4.4 displays the absolute vorticity of the bi-variate error field $\tilde{x}_2(\theta) - x_2(\theta)$ de-

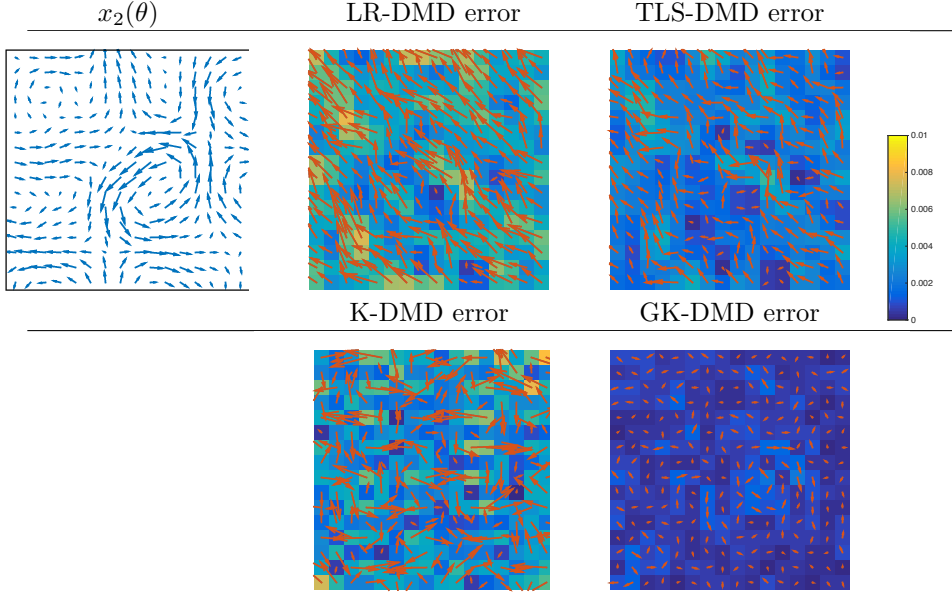


FIG. 4.5. Reconstruction errors maps of the different ROM approximations for $k = 70$. The vector field at upper left corner is related to the snapshot $x_2(\theta)$ for a typical initial condition θ , while other vector fields enlarged at scale 20:1 are related to the reconstruction error $\tilde{x}_2(\theta) - x_2(\theta)$ superimposed on the maps of the absolute error $|\tilde{x}_2(\theta) - x_2(\theta)|$.

finned over the bi-dimensional grid, where $\tilde{x}_2(\theta)$ denotes the approximation provided by the algorithms for a given initial condition θ . Error maps are displayed for increasing value of the dimension k . The distribution of the error produced by K-DMD reveals that its chaotic behavior as k increases is caused by error in a wide range of scales. Error maps obtained with the LR-DMD and TLS-DMD algorithms are very similar. Moreover they seem not to evolve significantly as k increases, except for high frequency appearing at $k \geq 10$. The error maps for GK-DMD show that the decrease in error with respect to k is related to refinements occurring at increasingly finer scales. Interestingly, the simplified turbulence model confirms this scale analysis of errors. In Figure 4.5, we observe that the large vortices of the flow are correctly approximated by GK-DMD for $k = 70$. By contrast, GK-DMD does not reconstruct accurately less energetic small vortices of the divergence-free fBm. Although TLS-DMD produces a reasonable error, we remark that TLS-DMD and LR-DMD clearly fail at identifying some of the large structures of the flow. The inspection of error maps produced by K-DMD reveal large errors at all scales, and its inaccuracy for reduced modeling of the fractal structure of turbulence.

4.2.3. Robustness to Overfitting. We pointed out in the previous analysis that LR-DMD and TLS-DMD might be prone to overfitting, while kernel methods seem to be more robust. We now discuss this point by evaluating the learning error ϵ_{learn} as a function of the reduced model dimension k for the approximation of Rayleigh-Bénard convection. Curves illustrating the learning error attained by the four algorithms are presented in Figure 4.6.

The plot of Figure 4.6 shows that LR-DMD, TLS-DMD or GK-DMD perform good and similarly in terms of learning error up to $k \sim 7$ (while K-DMD fails completely). From then, the learning error is continuously reduced as k grows by LR-DMD and TLS-DMD, while GK-DMD reaches an asymptote (the same as K-DMD from $k = 17$). We point out that the gain of LR-DMD and TLS-DMD compared to

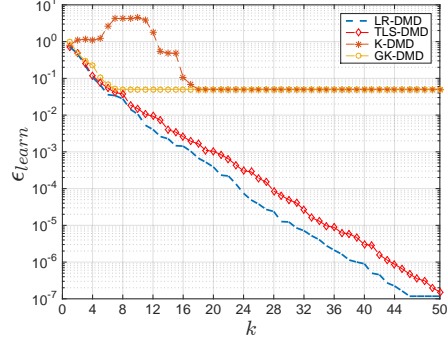


FIG. 4.6. *Evaluation of learning error ϵ_{learn} as a function of the dimension k of the reduced-model approximation, for a Gaussian kernel.*

GK-DMD reaches more than 5 decades at $k = 50$. Noticing that, on the contrary to this continuous decrease of the learning error, the reconstruction error of LR-DMD and TLS-DMD in Figure 4.2 stagnates for $k \geq 7$, we conclude that these methods overfit the training samples. GK-DMD and K-DMD seem in our experiments relieved up to some extent of this inconvenience. The observed robustness of kernel methods is in accordance with empirical results obtained for K-DMD in [24]: in their numerical simulations the authors showed that immersing the dynamics in the high-dimensional space \mathcal{H} enhanced the eigen-values estimates by lowering their variance and discarding neglectible ones.

4.2.4. Robustness to Noise. We assess the robustness of the reduced models by evaluating the learning error ϵ_{learn} in the noiseless case or in the case of an additive Gaussian noise of increasing variance. We consider the approximation of Rayleigh-Bénard convection. Figure 4.7 presents the learning error as a function of the reduced model dimension. We observe that performances of kernel-based methods, and particularly GK-DMD, seem to be weakly sensitive to the power of the additive noise. On the contrary, we remark a significant increase of the learning error for LR-DMD or TLS-DMD in the presence of noise. This deterioration is accentuated by the noise power. However, comparing the curves in Figure 4.2 and Figure 4.7, we notice that the reconstruction error ϵ_{rec} of LR-DMD and TLS-DMD is lower in the presence of noise, and thus that an additive noise in the learning phase increases the prediction capabilities of these two reduced models. This behavior is likely to be the consequence of overfitting. On the contrary, in the case of a noisy setting, the analysis of the reconstruction error confirms that the reduced model learned by GK-DMD is relevant for prediction. In particular, results in Figure 4.7 are consistent with those obtained in a noiseless setting in Figure 4.2. In particular, GK-DMD outperforms in terms of accuracy the other methods for $k \leq 16$.

5. Conclusion. This work presents a data-driven algorithm for the tractable approximation of a linear low-rank operator characterizing dynamics embedded in a RKHS. Taking advantage of the reproducing kernel property, the algorithm computes off-line a low-dimensional spectral representation of the solution of a low-rank constrained optimization problem, and then solves on-line a minimum distance problem which yields the sought approximation. By contrast to existing algorithms, the

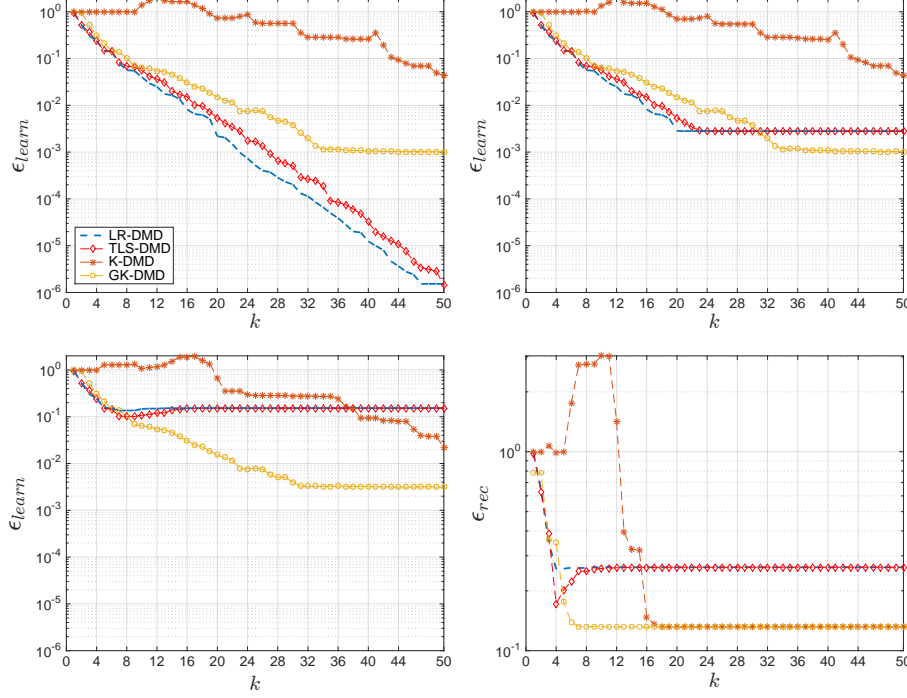


FIG. 4.7. Evaluation of errors ϵ_{learn} and ϵ_{rec} as a function of the dimension k of the reduced-model approximation using a Gaussian kernel and different levels of additive Gaussian noise: ϵ_{learn} for signal-to-noise ratio equal to ∞ (upper left), 54 (upper right) or 34 (lower left); ϵ_{rec} for signal-to-noise ratio equal to 54 (lower right).

proposed reduced model exhibits a low computational complexity and requires mild assumptions. Numerical simulations illustrate the gain in accuracy allowed by the proposed algorithm in the case of a meteorological system and a turbulence model.

Appendix A. The K-DMD algorithm.

Interested readers may find in this section a precise description of the K-DMD algorithm introduced in [24]. K-DMD is exposed in Algorithm 2. We discuss hereafter its different steps and then make some comments on its complexity.

First, K-DMD computes matrices in step 1), relying on the kernel-trick. Next, in step 2), 3) and 6), K-DMD relies on the assumption that $A_k^* = \hat{A}_k^{\ell s}$ and that we can identify the left eigen-vectors of $\hat{A}_k^{\ell s}$ as $\{\xi_i = U_{\Psi_{\mathbf{X}}} \tilde{\xi}_i\}_{i=1}^m$ and its eigen-values as $\{\lambda_i = \tilde{\lambda}_i\}_{i=1}^m$. Here, $\{\tilde{\xi}_i\}_{i=1}^m$ and $\{\tilde{\lambda}_i\}_{i=1}^m$ denote the right eigen-vectors and eigen-values of the matrix $R(\Psi_Y^* \Psi_X)R^* \in \mathbb{R}^{m \times m}$ with $R = \Sigma_{\Psi_{\mathbf{X}}}^\dagger V_{\Psi_{\mathbf{X}}}^*$. As shown by simple algebraic manipulations and using Proposition 3.1, the previous identification of eigen-vectors and eigen-values holds in the particular case where $k = m$ (assumption i) and $\Psi_{\mathbf{X}}$ is full rank (assumption ii). In this particular case, using the fact that $U_{\Psi_{\mathbf{X}}} = \Psi_{\mathbf{X}} R^*$, the i -th eigen-function approximation $\varphi_i(\theta)$ can be evaluated at any point $\theta \in \mathbb{R}^p$ as $\varphi_i(\theta) = \langle \xi_i, \Psi(\theta) \rangle_{\mathcal{H}} = \tilde{\xi}_i^* R \Psi_{\mathbf{X}}^* \Psi(\theta)$.

Then, the algorithm approximates the μ_j 's in reduced model (2.4), with the underlying assumption that Ψ^{-1} is linear (assumption iii). In steps 7), K-DMD identifies

Algorithm 2 : K-DMD [24]

• Off-line

Inputs: the $x_t(\vartheta_i)$'s

- 1) Compute matrices $\Psi_{\mathbf{X}}^* \Psi_{\mathbf{X}}$, $\Psi_{\mathbf{Y}}^* \Psi_{\mathbf{X}}$ in $\mathbb{R}^{m \times m}$ with the kernel trick.
 - 2) Get $(V_{\Psi_{\mathbf{X}}}, \Sigma_{\Psi_{\mathbf{X}}})$ by eigen-decomposition of $\Psi_{\mathbf{X}}^* \Psi_{\mathbf{X}}$.
 - 3) Compute the eigen-vectors $\{\tilde{\xi}_i\}_{i=1}^m$ and eigen-values $\{\tilde{\lambda}_i\}_{i=1}^m$ of $R \Psi_{\mathbf{Y}}^* \Psi_{\mathbf{X}} R^*$, with $R = \Sigma_{\Psi_{\mathbf{X}}}^\dagger V_{\Psi_{\mathbf{X}}}^*$.
 - 4) Compute the pseudo-inverse $((\tilde{\xi}_1 \cdots \tilde{\xi}_m)^*)^\dagger$.
- Outputs:** R , $\tilde{\xi}_i$'s, $\tilde{\lambda}_i$'s and $((\tilde{\xi}_1 \cdots \tilde{\xi}_m)^*)^\dagger$

• On-line

Inputs: off-line outputs and a given θ

- 5) Compute $\Psi_{\mathbf{X}}^* \Psi(\theta)$ in \mathbb{R}^m with the kernel trick.
- 6) Estimate eigen-functions $\{\varphi_i(\theta)\}_{i=1}^m$ using (3.3).
- 7) Estimate eigen-modes $\{\mu_i\}_{i=1}^m$ using (A.1).
- 8) Compute $\tilde{x}_T(\theta)$ using (2.4) with $\nu_{i,T} = \tilde{\lambda}_i^{T-1} \varphi_i(\theta)$.

Output: $\tilde{x}_T(\theta)$.

the μ_j 's as the minimizers in \mathbb{C}^p of the square of the ℓ_2 -norm of the reduced model error $\|x_{t+1}(\vartheta_i) - \sum_{j=1}^m \mu_j \lambda_j \langle \xi_j, \Psi(x_t(\vartheta_i)) \rangle_{\mathcal{H}}\|_2^2$ for any data pair $(x_t(\vartheta_i), x_{t+1}(\vartheta_i))$ satisfying (1.1). The authors thus implicitly assume that the eigen-modes belong to a sub-space in the span of \mathbf{Y} (assumption *iv*). We notice that by using (3.3), where $\Psi(\theta)$ is substituted by $\Psi(x_t(\vartheta_i))$ for $i \in 1, \dots, N$ and $j \in 1, \dots, T' - 1$, we have for $i = 1, \dots, m$ that $(\langle \xi_i, \Psi(x_1(\vartheta_1)) \rangle_{\mathcal{H}} \cdots \langle \xi_i, \Psi(x_{T'-1}(\vartheta_N)) \rangle_{\mathcal{H}}) = \tilde{\xi}_i^* \Sigma_{\Psi_{\mathbf{X}}} V_{\Psi_{\mathbf{X}}}^*$. The estimated $\hat{\mu}_j$'s are thus rewritten as the solution of

$$\arg \min_{\mu_1, \dots, \mu_m} \|\mathbf{Y} - (\mu_1 \cdots \mu_m) \text{diag}(\tilde{\lambda}_1 \cdots \tilde{\lambda}_m) (\tilde{\xi}_1 \cdots \tilde{\xi}_m)^* \Sigma_{\Psi_{\mathbf{X}}} V_{\Psi_{\mathbf{X}}}^*\|_{\mathcal{HS}},$$

where we remark that the Hilbert-Schmidt norm $\|\cdot\|_{\mathcal{HS}}$ boils down here to the Frobenius norm of a matrix in $\mathbb{R}^{p \times m}$. A minimizer of this least-square optimization problem is

$$(\hat{\mu}_1 \cdots \hat{\mu}_m) = \mathbf{Y} R^* ((\tilde{\xi}_1 \cdots \tilde{\xi}_m)^*)^\dagger \text{diag}(\tilde{\lambda}_1^\dagger \cdots \tilde{\lambda}_m^\dagger). \quad (\text{A.1})$$

Finally, using the identification $\{\lambda_i = \tilde{\lambda}_i\}_{i=1}^k$, the k first eigen-modes estimates $\{\hat{\mu}_i\}_{i=1}^k$ in (A.1) with the $\varphi_i(\theta)$'s given by (3.3) fully parametrize (2.4), yielding the approximation $\tilde{x}_T(\theta) = \sum_{i=1}^k \lambda_i^{T-1} \varphi_i(\theta) \hat{\mu}_i$.

The suitability of K-DMD for reduced modeling is weak in the case $k < m$ and $p \gg 1$. Indeed, we can show that the computation burden to compute the approximation is independent of the reduced model dimension k , but requires m^2 vector operations in \mathbb{R}^p . More precisely, the overall complexity of the K-DMD algorithm may be divided in an *on-line* and *off-line* part, defined as the complexity of the steps respectively independent or not of the initial condition θ we want to evaluate. We observe that the off-line part requires $\mathcal{O}(m^2(m+p))$ operations to compute the matrix products in step 1), the eigen-decompositions in steps 2) and 3) and the pseudo-inversion in step 4), while the on-line part requires $\mathcal{O}(pm^2)$ operations to compute the least-square solution in step 7). Thus the on-line computation is lighter than the off-line one but the complexity is in $\mathcal{O}(pm^2)$ whatever the reduced model dimension. A consequence is that the lower k , the higher the ratio complexity/accuracy, which is

obviously not a desirable property for reduced modeling.

Appendix B. Proof of Proposition 1. Let

$$\tilde{A}_{\ell,k} = (R \Psi_Y^* \Psi_Y S_k^* S_k \Psi_Y^* \Psi_X R^*)^* \quad \text{and} \quad \tilde{A}_{r,k} = S_k \Psi_Y^* \Psi_Y R^* R \Psi_X^* \Psi_Y S_k^*.$$

We begin by proving that the $U_{\Psi_X} \tilde{\xi}_i$'s are right eigen-vectors of $(A_k^*)^*$. We verify after some algebraic manipulations that $U_{\Psi_X}^* (A_k^*)^* U_{\Psi_X} = (\tilde{A}_{\ell,k})^*$. Then, as U_{Ψ_X} is unitary we have $(A_k^*)^* U_{\Psi_X} = U_{\Psi_X} (\tilde{A}_{\ell,k})^*$, and in particular $(A_k^*)^* U_{\Psi_X} \tilde{\xi}_i = U_{\Psi_X} (\tilde{A}_{\ell,k})^* \tilde{\xi}_i$. Exploiting the fact that $(\tilde{\xi}_i, \tilde{\lambda}_i)$ are eigen-vectors and eigen-values of $(\tilde{A}_{\ell,k})^*$, we obtain for $i = 1, \dots, k$ the sought result: $(A_k^*)^* U_{\Psi_X} \tilde{\xi}_i = \tilde{\lambda}_i U_{\Psi_X} \tilde{\xi}_i$.

We continue by showing that the $\hat{P}_k \tilde{\zeta}_i$'s are right eigen-vectors of A_k^* . From the definition of A_k^* and $\tilde{A}_{r,k}$ we obtain $\hat{P}_k^* A_k^* \hat{P}_k = \tilde{A}_{r,k}$. Then, $\hat{P}_k \hat{P}_k^* A_k^* \hat{P}_k = \hat{P}_k \tilde{A}_{r,k}$, which can be rewritten as $A_k^* \hat{P}_k = \hat{P}_k \tilde{A}_{r,k}$, since matrix $\hat{P}_k \hat{P}_k^*$ is idempotent and $\hat{P}_k \hat{P}_k^* A_k^* = \hat{P}_k \hat{P}_k^* \hat{P}_k \hat{P}_k^* \Psi_Y \Psi_X^\dagger = A_k^*$. Because $\tilde{\zeta}_i$ are eigen-vectors of $\tilde{A}_{r,k}$, we deduce for $i = 1, \dots, k$ the sought result: $A_k^* \hat{P}_k \tilde{\zeta}_i = \tilde{\lambda}_i \hat{P}_k \tilde{\zeta}_i$. \square

Appendix C. Inverse Mapping.

C.1. Extended Definition. In this section, we first show that there exists an implicit definition of the inverse mapping for any element of the subset $\mathcal{S} = \{x \in \mathcal{H} : x = \Psi(y), y \in \mathbb{R}^p\} \subseteq \mathcal{H}$, where we recall that \mathcal{H} is an RKHS characterized by the reproducing kernel

$$\forall (y, z) \in \mathbb{R}^p \times \mathbb{R}^p, \quad h(y, z) = \langle \Psi(y), \Psi(z) \rangle_{\mathcal{H}}. \quad (\text{C.1})$$

We then propose an extension of this definition for any element of \mathcal{H} .

First, let us show that the inverse of any $\eta \in \mathcal{S}$, $\Psi^{-1}(\eta)$ is implicitly defined as the unique element of \mathbb{R}^p given by

$$\Psi^{-1}(\eta) = \arg \max_{z \in \mathbb{R}^p} \frac{\langle \eta, \Psi(z) \rangle_{\mathcal{H}}}{\|\Psi(z)\|_{\mathcal{H}}}. \quad (\text{C.2})$$

Indeed, the positive-definiteness of the kernel h implies that we have for any $y, z \in \mathbb{R}^p$

$$\det \begin{pmatrix} h(y, y) & h(y, z) \\ h(z, y) & h(z, z) \end{pmatrix} \geq 0,$$

and the lower bound is reached if and only if $y = z$. Using the kernel symmetry, this is equivalent to

$$\frac{h(y, z)^2}{h(y, y)h(z, z)} \leq 1,$$

and, according to (C.1), it follows that

$$\frac{\langle \Psi(y), \Psi(z) \rangle_{\mathcal{H}}^2}{\|\Psi(y)\|_{\mathcal{H}}^2 \|\Psi(z)\|_{\mathcal{H}}^2} \leq 1, \quad (\text{C.3})$$

for any $y, z \in \mathbb{R}^p$ where the upper bound is reached if and only if $y = z$. (C.3) then implies definition (C.2).

Then, as proposed in (2.2), we extend definition (C.2) holding for elements of \mathcal{S} to any η in \mathcal{H} (i.e., including elements outside \mathcal{S}), as an element $\Psi^{-1}(\eta)$ of \mathbb{R}^p satisfying

$$\Psi^{-1}(\eta) \in \arg \min_{z \in \mathbb{R}^p} \|\eta - \Psi(z)\|_{\mathcal{H}}. \quad (\text{C.4})$$

The definition (C.2) coincides with definition (C.4) for normalized kernels (or more generally if $\|\Psi(z)\|_{\mathcal{H}} = \text{cte}$).

C.2. Sufficient Conditions for Existence. In this section, we provide a set of mild sufficient conditions so that the inverse $\Psi^{-1}(\sum_{i=1}^m g_i^{\theta,T} \Psi(y_i))$ exists, Ψ^{-1} being defined in (C.4). This inverse is involved in (3.6) and was reformulated as the problem of the existence of a vector $z^* \in \mathbb{R}^p$ satisfying $f(z^*) = \inf_{z \in \mathbb{R}^p} f(z)$, where the objective function is $f(z) = h(z, z) - 2 \sum_{i=1}^m g_i^{\theta,T} h(y_i, z)$.

PROPOSITION C.1. *A vector $\arg \inf_{z \in \mathbb{R}^p} f(z)$ exists if one of the two following conditions holds.*

- (1) *$f(z)$ is coercive and lower semicontinuous.*
- (2) *i) $h(x, x)$ is constant for any $x \in \mathbb{R}^p$,
ii) $\lim_{\|z\| \rightarrow \infty} h(x, z) = 0$ for any $x \in \mathbb{R}^p$,
iii) $\int_{\mathbb{R}^p} h(x, z) dz = c$ with $c \geq 0$ constant for any $x \in \mathbb{R}^p$,
iv) $f(z)$ is lower semicontinuous,
v) $\sum_{i=1}^m g_i^{\theta,T} > 0$.*

Proof of condition (1). As \mathbb{R}^p is closed, the Weierstrass' Theorem [1, Proposition A.8] states that a minimizer exists under condition (1). \square

Proof of condition (2). Under condition (2-i), we have

$$\arg \inf_{z \in \mathbb{R}^p} f(z) = \arg \inf_{z \in \mathbb{R}^p} \left(- \sum_{i=1}^m g_i^{\theta,T} h(y_i, z) \right), \quad (\text{C.5})$$

and condition (2-ii) implies that for $i = 1 \dots, m$ we have

$$\lim_{\|z\| \rightarrow \infty} - \sum_{i=1}^m g_i^{\theta,T} h(y_i, z) = 0. \quad (\text{C.6})$$

Moreover, under conditions (2-iii) and (2-v),

$$\exists z^* \in \mathbb{R}^p \quad \text{such that} \quad - \sum_{i=1}^m g_i^{\theta,T} h(y_i, z^*) < 0. \quad (\text{C.7})$$

Indeed, by contraposition, assume that $-\sum_{i=1}^m g_i^{\theta,T} h(y_i, z) \geq 0$ for all $z \in \mathbb{R}^p$. By integrating with respect to z , as each term in the sum is independent of the point y_i under condition (2-iii), we obtain that $-c \sum_{i=1}^m g_i^{\theta,T} \leq 0$ and as $c \geq 0$, that $\sum_{i=1}^m g_i^{\theta,T} \leq 0$, which contradicts (2-v).

The existence of a minimizer then follows from (C.5), (C.6), (C.7) and assumption (2-iv). Indeed, assume a sequence $\{x_k\} \subset \mathbb{R}^p$ such that $\lim_{k \rightarrow \infty} f(x_k) = \inf_{z \in \mathbb{R}^p} f(z)$. $\{x_k\}$ must be bounded since (C.5) and (C.6) show, that on the one hand the objective function $f(z)$ tends to 0 as the norm of z grows to infinity, and on the other hand (C.7) guarantees that there exists at least one point for which the objective function is negative. Using the lower semicontinuity of f , the proof then proceeds like the proof of the Weierstrass' Theorem [1, Proposition A.8]. \square

C.3. Examples. The sufficient conditions for existence of the inverse hold for several class of kernels. In particular, condition (1) holds for the polynomial kernels of the form $h(y_i, z) = (1 + y_i^* z)^\gamma$, $\gamma \in \mathbb{N}^*$. Indeed, the objective function $f(z) = (1 + \|z\|_2^2)^\gamma - 2 \sum_{i=1}^m g_i^{\theta,T} (1 + y_i^* z)^\gamma$ is in this case continuous and coercive since $\lim_{\|z\| \rightarrow \infty} f(z) = \lim_{\|z\| \rightarrow \infty} \|z\|_2^{2\gamma} = +\infty$. Conditions (2-i), (2-ii), (2-iii) and (2-iv)

are in particular verified for Gaussian kernels of the form $h(y_i, z) = \exp^{-\frac{1}{2\sigma^2} \|y_i - z\|_2^2}$ with $\sigma > 0$, or Laplacian kernels of the form $h(y_i, z) = \exp^{-\frac{1}{\beta} \|y_i - z\|_2}$ with $\beta > 0$. The existence of the inverse is therefore guaranteed for these kernels as long as we check that condition (2-v) holds. This positivity condition was always observed in our numerical simulations.

Appendix D. High-Dimensional Model and Experimental Setting.

We assess the different reduced modeling methods on two high-dimensional systems: first a standard geophysical model and then a toy model for turbulence exhibiting a fractal structure of vortices.

D.1. Rayleigh-Bénard Convection. Rayleigh-Bénard convection [3] is a standard benchmark model in meteorology. Convection is driven by two coupled partial differential equations. Let $\nabla = (\partial_{s_1}, \partial_{s_2})^*$, $\nabla^\perp = (\partial_{s_2}, -\partial_{s_1})^*$ and $\Delta = \partial_{s_1}^2 + \partial_{s_2}^2$ denote the gradient, the curl and the Laplacian with respect to the two spatial dimensions (s_1, s_2) . Boundary conditions are 1-periodic along s_1 and of Dirichlet type⁴ on s_2 . At any point of the unit cell $\mathbf{s} = (s_1, s_2) \in [0, 1]^2$ and for any time $t \geq 1$, the temperature $\tau(\mathbf{s}, t) \in \mathbb{R}$, the vorticity $b(\mathbf{s}, t) \in \mathbb{R}$ and the velocity $v(\mathbf{s}, t) \in \mathbb{R}^2$ in the cell satisfy

$$\begin{cases} \partial_t b(\mathbf{s}, t) + v(\mathbf{s}, t)^* \nabla b(\mathbf{s}, t) - \text{Pr} \Delta b(\mathbf{s}, t) - \text{Pr Ra} \partial_{s_1} \tau(\mathbf{s}, t) = 0, \\ \partial_t \tau(\mathbf{s}, t) + v(\mathbf{s}, t)^* \nabla \tau(\mathbf{s}, t) - \Delta \tau(\mathbf{s}, t) - \partial_{s_1} \Delta^{-1} b(\mathbf{s}, t) = 0, \end{cases}$$

where velocity is related to vorticity according to $v(\mathbf{s}, t) = \nabla^\perp \Delta^{-1} b(\mathbf{s}, t)$, and where Δ^{-1} represents the inverse of Δ defined in the Fourier domain. We set the Rayleigh number to $\text{Ra} = 1.5e5$ and the Prandtl number to $\text{Pr} = 1.0e1$. We use a Runge-Kutta fourth-order time discretization. For spatial discretization, we use a Fourier-based implementation of spatial derivatives except for the advection term for which we use a second-order finite difference scheme. We obtain a discrete system of the form of (1.1) with $x_t = (b_t, \tau_t)^* \in \mathbb{R}^p$, and $p = 4096$, where b_t 's and τ_t 's are spatial discretizations on a grid of size 64×32 of vorticity and temperature fields at time t . For time-integration of the dynamic model, we use a time step of $1e-4$. In our experiments, we assume that the initial condition belongs to the Lorenz attractor [16]. The initial state is of the form $b(\mathbf{s}, 1) = \kappa_b \sin(a_b s_1) \sin(\pi s_2)$, $\tau(\mathbf{s}, 1) = \kappa_{\tau_1} \cos(a_\tau s_1) \sin(\pi s_2) - \kappa_{\tau_2} \sin(2\pi s_2)$, with the parameter vector $(a_b, a_\tau, \kappa_b, \kappa_{\tau_1}, \kappa_{\tau_2}) \in \mathbb{R}^5$. In our experiments, we sample parameters using a uniform distribution on the hyper-cube $(a_b, a_\tau, \kappa_b, \kappa_{\tau_1}, \kappa_{\tau_2}) \in [0, 0.1]^5$.

D.2. Divergence-Free Fractional Brownian Motion Evolution. A simple model inspired by the turbulence phenomenology is proposed to evaluate the capability of reduced modeling methods to capture the motion fractal structure. The states $x_t(\vartheta_j)$ are discrete motion fields defined on a square grid. The states satisfy (1.1) with the quadratic model $f(x_t) = (x_{t-1} + 1)^2 + \alpha L x_{t-1} - 1$, where the square power is taken component-wise, the diffusion coefficient is $\alpha = 0.5$ and $L \in \mathbb{R}^{p \times p}$ is a second-order finite difference approximation of the (bi-variate) two-dimensional Laplacian operator. Each initial state is a sample from a bi-dimensional divergence-free fractional Brownian motion (fBm) field of Hurst exponent $1/3$. The ambient dimension is set to $p = 512$ and the size of the square grid is set 16×16 . The fBm vector fields are parametrized according to the fractional wavelet representation proposed in [10, Proposition 3.1], using 18 random coefficients drawn according to a normal law.

⁴In order to simplify the Fourier-based numerical implementation of the model, we will assume periodicity for the discretised system in the two spatial directions.

Acknowledgements. The authors would like to thank Mathias Rousset for his help in proving Proposition C.1.

REFERENCES

- [1] Bertsekas, D.: Nonlinear Programming. Athena Scientific (1995)
- [2] Bishop, C.M.: Pattern Recognition and Machine Learning (Information Science and Statistics). Springer-Verlag, Berlin, Heidelberg (2006)
- [3] Chandrasekhar, S.: Hydrodynamic and hydromagnetic stability. Courier Corporation (2013)
- [4] Chen, K.K., Tu, J.H., Rowley, C.W.: Variants of dynamic mode decomposition: boundary condition, koopman, and fourier analyses. *Journal of nonlinear science* **22**(6), 887–915 (2012)
- [5] Golub, G., Van Loan, C.: Matrix Computations. Johns Hopkins Studies in the Mathematical Sciences. Johns Hopkins University Press (2013)
- [6] Héas, P., Herzet, C.: Low rank dynamic mode decomposition: Optimal solution in polynomial time. *arXiv e-prints* (2017)
- [7] Héas, P., Herzet, C.: Optimal low-rank dynamic mode decomposition. In: 2017 IEEE International Conference on Acoustics, Speech and Signal Processing (ICASSP), pp. 4456–4460. IEEE (2017)
- [8] Héas, P., Herzet, C.: Low-rank approximation of linear maps. *arXiv e-prints* (2018)
- [9] Héas, P., Herzet, C., Combès, B.: Generalized kernel-based dynamic mode decomposition. In: IEEE International Conference on Acoustics, Speech and Signal Processing (ICASSP) (2020)
- [10] Héas, P., Lavancier, F., Kadri-Harouna, S.: Self-similar prior and wavelet bases for hidden incompressible turbulent motion. *SIAM Journal on Imaging Sciences* **7**(2), 1171–1209 (2014)
- [11] Hemati, M.S., Rowley, C.W., Deem, E.A., Cattafesta, L.N.: De-biasing the dynamic mode decomposition for applied Koopman spectral analysis of noisy datasets. *Theoretical and Computational Fluid Dynamics* **31**(4), 349–368 (2017)
- [12] Horn, R.A., Johnson, C.R.: Matrix analysis. Cambridge university press (2012)
- [13] Jovanovic, M., Schmid, P., Nichols, J.: Low-rank and sparse dynamic mode decomposition. *Center for Turbulence Research Annual Research Briefs* pp. 139–152 (2012)
- [14] Koopman, B.O.: Hamiltonian systems and transformation in hilbert space. *Proceedings of the National Academy of Sciences of the United States of America* **17**(5), 315 (1931)
- [15] Kowalski, K., Steeb, W.H.: Nonlinear dynamical systems and Carleman linearization. World Scientific (1991)
- [16] Lorenz, E.N.: Deterministic Nonperiodic Flow. *Journal of Atmospheric Sciences* **20**, 130–148 (1963)
- [17] Lusch, B., Kutz, J.N., Brunton, S.L.: Deep learning for universal linear embeddings of nonlinear dynamics. In: *Nature Communications* (2018)
- [18] Mezić, I., Banaszuk, A.: Comparison of systems with complex behavior. *Physica D: Nonlinear Phenomena* **197**(1-2), 101–133 (2004)
- [19] Nocedal, J., Wright, S.: Numerical Optimization. Springer Series in Operations Research and Financial Engineering. Springer New York (2000)
- [20] Schmid, P.J.: Dynamic mode decomposition of numerical and experimental data. *Journal of Fluid Mechanics* **656**, 5–28 (2010)
- [21] Steinwart, I., Hush, D., Scovel, C.: An explicit description of the reproducing kernel hilbert spaces of gaussian rbf kernels. *IEEE Transactions on Information Theory* **52**(10), 4635–4643 (2006)
- [22] Tu, J.H., Rowley, C.W., Luchtenburg, D.M., Brunton, S.L., Kutz, J.N.: On dynamic mode decomposition: Theory and applications. *Journal of Computational Dynamics* **1**(2), 391–421 (2014)
- [23] Williams, M.O., Kevrekidis, I., Rowley, C.: A data-driven approximation of the koopman operator: Extending dynamic mode decomposition. *Journal of Nonlinear Science* **25**(6), 1307–1346 (2015)
- [24] Williams, M.O., Rowley, C.W., Kevrekidis, I.G.: A kernel-based method for data-driven koopman spectral analysis. *Journal of Computational Dynamics* **2**(2), 247–265 (2015)
- [25] Yeung, E., Kundu, S., Hodas, N.: Learning deep neural network representations for koopman operators of nonlinear dynamical systems. In: 2019 American Control Conference (ACC), pp. 4832–4839. IEEE (2019)
- [26] Zhu, K.: Operator Theory in Function Spaces, Second Edition. Mathematical surveys and monographs. American Mathematical Soc. (2007)